

# Phase Equilibria in the TiO<sub>2</sub>-Rich Part of the TiO<sub>2</sub>-CaO-SiO<sub>2</sub>-10 Wt Pct Al<sub>2</sub>O<sub>3</sub>-5 Wt Pct MgO System at 1773 K



ZHEN WANG, QINGSHAN ZHU, and HAoyan SUN

The phase equilibria of the TiO<sub>2</sub>-CaO-SiO<sub>2</sub>-10 wt pct Al<sub>2</sub>O<sub>3</sub>-5 wt pct MgO system in the TiO<sub>2</sub>-rich part were investigated experimentally at 1773 K using the high-temperature equilibration–quenching method and the electron probe microanalyses. Through this study, the isothermal section of the above system was obtained containing one liquidus region and five solid–liquid coexistence regions. The primary phase region of anosovite was not only found, but it is the optimal composition region that is most beneficial to the anosovite selective crystallization and separation. The phase diagram of the TiO<sub>2</sub>-CaO-SiO<sub>2</sub>-10 wt pct Al<sub>2</sub>O<sub>3</sub>-5 wt pct MgO system in the TiO<sub>2</sub>-rich corner at 1773 K has been established. The obtained phase diagram can provide reliable reference for the slag adjusting during vanadium-titanium magnetites smelting to make sure the resulting Ti-bearing slag can be upgraded using the selective crystallization and phase separation method.

<https://doi.org/10.1007/s11663-018-1441-2>

© The Minerals, Metals & Materials Society and ASM International 2018

## I. INTRODUCTION

It is always a challenge for experts to exploit the plentiful titanium resources in vanadium-titanium magnetites. Various methods of the vanadium-titanium magnetites utilization have been developed, such as the blast furnace processes or the direct reduction-smelting processes. Through these methods, the utilization of the iron and vanadium components can be realized by being reduced into the hot metal, but most of the titanium resources are left in the slag to form Ti-bearing slag.<sup>[1–5]</sup> The utilization of the Ti-bearing slag is always a tough task, because the TiO<sub>2</sub> content is relatively low and the distribution of the Ti components in it is dispersal.<sup>[1–4]</sup> Fortunately, the above-mentioned direct reduction-smelting processes are more effective in concentrating the Ti components. By this method, titanium resources can be concentrated to the Ti-bearing slag containing 45 to 60 wt pct TiO<sub>2</sub>, which is much higher than the Ti-bearing slag (20 to 25 wt pct TiO<sub>2</sub>) from the

blast furnace processes. From this perspective, the development of direct reduction-smelting processes is fairly progressive. Even so, there are still relatively high levels of Al<sub>2</sub>O<sub>3</sub> and SiO<sub>2</sub> in the Ti-bearing slag from smelting processes. Consequently, on the one hand, there is little chance for this 45 to 60 wt pct TiO<sub>2</sub>-bearing slag to be used directly as a valuable material in other subsequent processes. On the other hand, this 45 to 60 wt pct TiO<sub>2</sub>-bearing slag remains difficult to be upgraded by most of the processing methods,<sup>[6–8]</sup> like the leaching processes.

Hopefully, some researches prove that the selective crystallization and phase separation method has an application prospect in the extraction of the vanadium/boron/titanium from the vanadium bearing slags/boron bearing slags/Ti-bearing blast furnace (Ti-BF) slag.<sup>[9–12]</sup> Inspired by this, the present authors preliminarily studied the upgradation of the 45 to 60 wt pct TiO<sub>2</sub>-bearing slag using the selective crystallization and phase separation method.<sup>[13]</sup> The study shows that by promoting the Ti components being enriched in the anosovite phase and the selective separation of the anosovite phase, the 45 to 60 wt pct TiO<sub>2</sub>-bearing slag can be upgraded to containing nearly 70 wt pct TiO<sub>2</sub>.<sup>[15]</sup> It is proved that anosovite phase is the optimal titanium phase for the selective crystallization and phase separation method.<sup>[13,14]</sup> Thus, selective crystallization of the anosovite phase is critical for the upgradation of the 45 to 60 wt pct TiO<sub>2</sub>-bearing slag using the selective crystallization and phase separation method.

ZHEN WANG and QINGSHAN ZHU are with the State Key Laboratory of Multiphase Complex Systems, Institute of Process Engineering, Chinese Academy of Sciences, Beijing 100190, China and also with the School of Chemical Engineering, University of Chinese Academy of Sciences, Beijing 100049, China. Contact e-mail: wangzhen@ipe.ac.cn HAoyan SUN is with the State Key Laboratory of Multiphase Complex Systems, Institute of Process Engineering, Chinese Academy of Sciences.

Manuscript submitted December 12, 2017.

Article published online October 31, 2018.

However, in practice, the chemical compositions of the slag change frequently with the change of the process parameters or source of raw ores. So, the main concern is how to adjust the composition of the slag during the smelting process to ensure the formation of the anosovite. Based on this point, the phase equilibrium diagram of the Ti-bearing slag is highly desirable. By constructing the phase diagram, the primary phase region of anosovite can be distinguished, which can be used as the guideline to adjust the composition of the Ti-bearing slag for anosovite precipitation.

Based on this, many researchers focus on the investigation on anosovite formation in the Ti-bearing slag. Wen *et al.* investigated and explained the important role of MgO in stabilizing the anosovite crystal structure.<sup>[15,16]</sup> Xirouchakis' theoretical research also gives some help in understanding the stability of MgTi<sub>2</sub>O<sub>5</sub>.<sup>[17]</sup> Seim and Kolbeinsen reported that the existing of MgO in slag is extremely important to the stability of anosovite.<sup>[18]</sup> Another research by the present authors indicates that MgO is the key component to promote the crystallization of anosovite.<sup>[13]</sup> Thus, it is essential to carry out the research on the phase equilibria of Ti-bearing slag containing MgO.

Yan *et al.* constructed the isothermal phase diagram of the MgO-SiO<sub>2</sub>-TiO<sub>x</sub> system at PO<sub>2</sub> of  $4.85 \times 10^{-11}$  atm and pointed out that the lower oxygen partial pressure is favorable to the formation of anosovite (Ti<sub>3-x</sub>Mg<sub>x</sub>O<sub>5</sub>).<sup>[19]</sup> But this system is relatively simple with the absence of CaO and Al<sub>2</sub>O<sub>3</sub>, which are important components in the real plant titanomagnetite slag and play significant influences in the formation of anosovite. Goso investigated the thermodynamic modeling in the 19.69 pct SiO<sub>2</sub>-13.12 pct Al<sub>2</sub>O<sub>3</sub>-37.19 pct TiO<sub>2</sub>-30 pct (CaO + MgO) system, finding a pseudobrookite solid solution (MgTi<sub>2</sub>O<sub>5</sub>-Al<sub>2</sub>TiO<sub>5</sub>) with high mass ratio of CaO + MgO and the increasing Ti<sup>3+</sup>/Ti<sup>4+</sup> mass fraction ratio with decreasing PO<sub>2</sub>.<sup>[20]</sup> But Goso's research are limited to the MgTi<sub>2</sub>O<sub>5</sub>-Al<sub>2</sub>TiO<sub>5</sub> solid solution, without Ti<sub>3</sub>O<sub>5</sub> (another important end-member to form anosovite under reducing conditions) being involved. Zhao *et al.* studied the liquidus temperatures and phase equilibria of the Al<sub>2</sub>O<sub>3</sub>-CaO-MgO-SiO<sub>2</sub>-TiO<sub>2</sub>-Ti<sub>2</sub>O<sub>3</sub> system applicable to blast furnace slag at low oxygen partial pressures to explore the possibility of recovering titanium resources in the form of pseudobrookite (a solid solution of MgO·2TiO<sub>2</sub>, Al<sub>2</sub>O<sub>3</sub>·TiO<sub>2</sub>, and Ti<sub>2</sub>O<sub>3</sub>·TiO<sub>2</sub>), and reported the presence of reduced titanium species Ti<sup>3+</sup> in the pseudobrookite phase.<sup>[21]</sup> Osborn *et al.* studied the phase equilibria in the system CaO-MgO-Al<sub>2</sub>O<sub>3</sub>-SiO<sub>2</sub>-TiO<sub>2</sub> to find out the characteristics of the Ti-BF slag during and after cooling.<sup>[22]</sup> Sun *et al.* obtained the phase relations of various CaO-SiO<sub>2</sub>-MgO-Al<sub>2</sub>O<sub>3</sub>-TiO<sub>2</sub> system relevant to high Al<sub>2</sub>O<sub>3</sub> Ti-bearing slag, and anosovite phase was found in the CaO-SiO<sub>2</sub>-5 wt pct MgO-30 wt pct Al<sub>2</sub>O<sub>3</sub>-TiO<sub>2</sub> system.<sup>[23-25]</sup> However, the above-mentioned Zhao's, Osborn's, as well as Sun's investigations mainly concern on the Ti-BF slag with low TiO<sub>2</sub> level, which is quite different from the composition of the current slag (TiO<sub>2</sub> > 45 pct). In some other research projects on the

titanomagnetite smelting type slags, the liquidus temperatures and the effects of SiO<sub>2</sub>, CaO, MgO on liquidus temperatures were investigated comprehensively to obtain the liquidus line of the phase diagram.<sup>[26,27]</sup> But these studies mainly focused on the liquidus temperatures, and the distribution of different phase region was not constructed.

In a word, the previous studies hardly give useful information about the phase equilibria characteristics of the current 45 to 60 wt pct TiO<sub>2</sub>-bearing slag, and the composition region for anosovite selective crystallization is not available in these reported phase diagrams. The studies on the phase equilibria of the 45 to 60 wt pct TiO<sub>2</sub>-bearing titanium slag are far from sufficient. It is urgent to carry out this research to realize the recovery of titanium resources from the direct reduction-smelting Ti-bearing slag by the selective crystallization and phase separation method.

Therefore, the objective of the present work is to carry out the study on the phase equilibria of TiO<sub>2</sub>-CaO-SiO<sub>2</sub>-Al<sub>2</sub>O<sub>3</sub>-MgO system. This study can not only ascertain the primary phase region of anosovite, but also give the distribution of different phase regions in the TiO<sub>2</sub>-rich part of the TiO<sub>2</sub>-CaO-SiO<sub>2</sub>-Al<sub>2</sub>O<sub>3</sub>-MgO system. The phase equilibria data of the Ti-bearing slag from the vanadium-titanium magnetites direct reduction-smelting processes will be greatly enriched. Based on the industrially practical composition of this Ti-bearing slag, the content of MgO and Al<sub>2</sub>O<sub>3</sub> is fixed at 5 and 10 wt pct, respectively.

## II. EXPERIMENTAL

### A. Sample Preparation

In this study, TiO<sub>2</sub>, CaCO<sub>3</sub>, SiO<sub>2</sub>, MgO, and Al<sub>2</sub>O<sub>3</sub> were used as the starting materials. And CaCO<sub>3</sub> was used as the starting material to avoid the weighing inaccuracy of CaO. At the experiment temperature (1773 K) of this work, CaCO<sub>3</sub> can be decarbonated (> 1173 K) completely in the sample. All the reagents were of analytical reagent grade from Sinopharm Chemical Reagent Co., Ltd, China. In the preparation of sample, each powder reagent was weighed to an accuracy of 0.0001 g, and then the five components with a certain proportion were mixed thoroughly in an agate mortar to obtain an experimental sample.

### B. Experimental Process

It is reported that, due to the high viscosities and the sluggishness of crystallization, the liquid phase in the silica-containing melts can be retained as glass on quenching.<sup>[28]</sup> Thus, it is reliable to use the quenching technique to investigate the phase equilibria of the silica-containing slag. In this study, the classical melting-high-temperature equilibration-quenching method was used to carry out the investigation on the phase equilibria of the TiO<sub>2</sub>-CaO-SiO<sub>2</sub>-10 wt pct Al<sub>2</sub>O<sub>3</sub>-5 wt pct MgO system.

Each powder sample was placed into a molybdenum crucible. The molybdenum crucible with a sample inside was placed into a carbon crucible which was suspended by a molybdenum wire in the even temperature zone of the furnace. After that, the sample was heated to be molten at 1873 K, and held at 1873 K for 2 hours to make sure complete melting and homogenization. Then the temperature fell from 1873 K to 1773 K, and the sample was held at 1773 K for 12 hours to obtain fully equilibration. Thereafter, the sample at 1773 K was quenched following the method below: the molybdenum wire was cut, so the sample was dropped directly into water placed under the furnace. The vertical tube furnace would allow this process be finished within a second, retaining the phases state at the equilibrium temperature. Finally, the quenched sample was washed with ethanol and dried. By observing the inner wall surface of the molybdenum crucible and the quenched sample edge near the crucible wall using a scanning electron microscope (SEM), it is known that there is no reaction between the molybdenum crucible and the sample.

The equilibration experiments were carried out in a low oxygen partial pressure atmosphere. Due to the use of the carbon crucible and the protection of argon, the gases in the furnace tube are mainly Ar, CO, and CO<sub>2</sub>, and the pO<sub>2</sub> is about  $5.87 \times 10^{-11}$  atm, which are determined using the qualitative and quantitative analysis by gas mass spectrometry method.

### C. Phase Identification

The phases in the quenched samples were detected by a SEM-energy dispersive X-ray spectrometer (EDS), an X-ray diffractometer (XRD), and the electron probe microanalysis (EPMA). The XRD patterns were obtained using a PANalytical X-ray diffractometer (PRO MPD, PANalytical B.V., The Netherlands). Part of each quenched sample was crushed and grinded into powders to do the XRD analysis.

For the SEM-EDS and EPMA analysis, each quenched sample (typical size: 8 mm × 8 mm × 5 mm) was remounted into epoxy resin, and polished to obtain a proper surface. After polishing, the surface of the sample was coated with carbon to ensure good electric conductivity. The SEM measurements were conducted using a ZEISS EVO MA18 microscope supporting an energy dispersive X-ray spectrometer (model: INCA X-MAX). Besides the phase identification, the EPMA analysis was also used to acquire the quantitative information of the glass phase in each sample to identify the composition of liquidus point. For accuracy, six analysis points in one glass phase were randomly chosen for each sample. The EPMA studies were conducted using a JEOL JXA-8230 microprobe (JEOL Ltd., Peabody, CA) equipped with four wavelength dispersive spectrometers. And the EPMA measurement conditions were as follows: an accelerating potential of 20 kV, a beam current of  $10^{-8}$  A, and a probe diameter of 1 μm. The compositions of TiO<sub>2</sub>, MgO, CaO, SiO<sub>2</sub>, and Al<sub>2</sub>O<sub>3</sub> were calculated using the ZAF correction method.

## III. RESULTS AND DISCUSSION

### A. Temperature Calibration and Equilibrium Identification

The method of temperature calibration and equilibrium identification is the same as that was described in our previous paper.<sup>[29]</sup> The brief introduction is as follows.

Slag of 51.7 wt pct SiO<sub>2</sub>-48.3 wt pct CaO (the composition of wollastonite) was selected as the reference sample to do the temperature calibration. Setting the furnace temperature equals real melting temperature of wollastonite (1817 K), then the difference between this setting value and 1817 K is the deviation. And the furnace temperature can be set according to this deviation in the following experiments.

As for the equilibrium identification, an optional quenched sample was analyzed by the SEM-EDS line scanning to obtain the elements distribution. It showed that the content of Ti/Ca/Si/Al/Mg element in glass phase exhibited no considerable variation with the distance from precipitates. That is, the sample was in equilibrium before quenching and no precipitation occurred during quenching. Thus, according to Jak *et al.*'s method,<sup>[28]</sup> the experimental procedure of this research is reliable.

### B. Valence State of Titanium Element

In this study, the carbon crucible can supply a reducing condition for the experimental process. Some of the Ti<sup>4+</sup> may be reduced. Thus, the quenched samples were measured by X-ray photoelectron spectroscopy (XPS, ESCALAB 250Xi from Thermo Fisher Scientific) to obtain the valence state of Ti and identify the reduction of Ti<sup>4+</sup>. A typical XPS pattern of Ti element for the quenched sample has been presented in Figure 1. It can be seen that a certain percentage of Ti<sup>3+</sup> exists in the sample. The reducing condition is effective. In the samples of this work, the Ti element mainly shows two valence states, Ti<sup>4+</sup> and Ti<sup>3+</sup>.

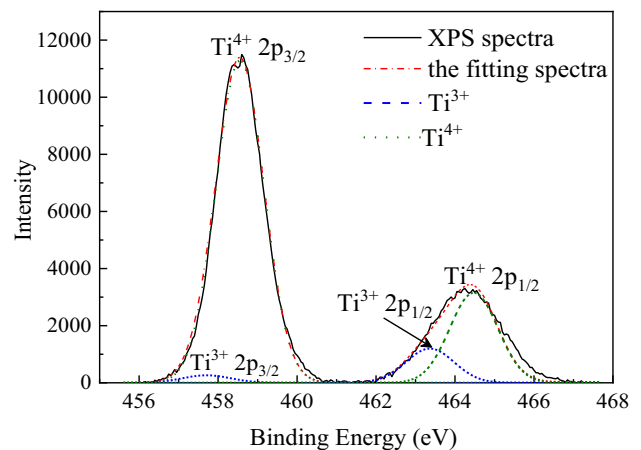


Fig. 1—A typical XPS background-subtracted spectra of Ti element for the quenched sample.

### C. Primary Phase Region of Perovskite

Table I shows the compositions of the experimental samples, the glass phase composition obtained by EPMA in each quenched sample, and the phases found in the primary phase region of perovskite at 1773 K. A total of 18 samples were studied in the present phase region, containing 6 liquid samples and 12 liquid-perovskite co-existing samples. It can be seen from Table I that the differences between composition value analyzed by EPMA and the prepared composition value for each liquid sample are minor, demonstrating that the relatively high accuracy of the EPMA analysis and the equilibrium state of the sample. An example (sample: 41 wt pct TiO<sub>2</sub>-25.5 wt pct CaO-18.5 wt pct SiO<sub>2</sub>-10 wt pct Al<sub>2</sub>O<sub>3</sub>-5 wt pct MgO) of the SEM-backscattered electron (BSE) micrograph and the XRD pattern for liquid sample at 1773 K is presented in Figure 2. No crystal observed in the SEM micrograph and no diffraction peak in the XRD pattern confirm the only existence of glass phase in the quenched sample. An example (sample: 46 wt pct TiO<sub>2</sub>-29 wt pct CaO-10 wt pct SiO<sub>2</sub>-10 wt pct Al<sub>2</sub>O<sub>3</sub>-5 wt pct MgO) of the SEM-BSE micrograph and the XRD pattern for liquid-perovskite coexistence equilibrium at 1773 K is presented in Figure 3. In Figure 3, the light grey phase is identified as perovskite based on a combination analysis of the SEM-EDS and the XRD results, and the dark grey phase is designated as the quenched glass phase. By the EPMA quantitative analysis on the quenched glass phase in the liquid-perovskite co-existing samples, the corresponding liquid composition for each liquid-solid co-existing sample can be determined. Thereafter, the corresponding liquid points in the isotherm are identified.

Nevertheless, it is worth noting that the content of MgO and Al<sub>2</sub>O<sub>3</sub> has been fixed at 5 pct and 10 wt pct, respectively, in the preparation of the samples; however, with the precipitation of some crystals from the slag in liquid-solid co-existing samples, both the content levels of MgO and Al<sub>2</sub>O<sub>3</sub> in the quenched glass phase are impossible to stay at 5 pct and 10 wt pct exactly. So, it is necessary to do a normalization of the quenched glass phase composition when a graphical presentation of the phase equilibrate data is drawn. The normalization processing is carried out as follows: the content of MgO and Al<sub>2</sub>O<sub>3</sub> is adjusted to 5 and 10 wt pct, respectively, and the compositions of the other three components are normalized with a sum of 85 wt pct in proportion to their original fractions. This normalization processing can inevitably lead to deviation between the true liquidus surface and the normalized data. The more deviation of MgO and Al<sub>2</sub>O<sub>3</sub> content from 5 and 10 wt pct, the larger deviation of the normalized data from the true liquidus surface. Thus, when the graphical presentation is done, only the experimental points with minor MgO and Al<sub>2</sub>O<sub>3</sub> content deviation from 5 and 10 wt pct are worthy of being normalized so as to avoid the deviation as much as possible. In this regard, in Table I, for the liquid-perovskite co-existing samples close to the liquid samples, such as No. 1 and Nos. 4 to 7, only trace amounts of perovskite precipitate without causing much visible changes on the content of MgO and Al<sub>2</sub>O<sub>3</sub> in glass phase. So, these samples are subjected to the quantitative analysis of the quenched glass phase by EPMA to obtain the corresponding liquid composition so that the liquid points in the isotherm are identified. While for the liquid-perovskite co-existing samples far from the liquid samples, such as Nos. 2 to 3 and Nos. 8 to 12, the crystallization of a

**Table I. Compositions of the Experimental Samples and the Glass Phase in Some Quenched Samples in the Primary Phase Region of Perovskite**

Nos.	Composition of the Experimental Sample (Weight Percent)					Phases Present	Glass Phase Composition Obtained by EPMA in Each Quenched Sample (Weight Percent)				
	TiO <sub>2</sub>	SiO <sub>2</sub>	CaO	Al <sub>2</sub> O <sub>3</sub>	MgO		TiO <sub>2</sub>	SiO <sub>2</sub>	CaO	Al <sub>2</sub> O <sub>3</sub>	MgO
1	35.00	20.00	30.00	10.00	5.00	L* + CT**	33.86	21.35	29.64	10.11	5.04
2	38.25	17.85	28.90	10.00	5.00	L + CT	—	—	—	—	—
3	42.50	15.30	27.20	10.00	5.00	L + CT	—	—	—	—	—
4	38.25	18.42	28.33	10.00	5.00	L + CT	37.53	19.51	28.10	9.94	4.92
5	40.50	17.25	27.25	10.00	5.00	L + CT	39.89	18.20	26.66	10.10	5.15
6	42.50	16.06	26.44	10.00	5.00	L + CT	41.48	17.19	25.99	10.28	5.06
7	45.90	13.60	25.50	10.00	5.00	L + CT	45.34	15.01	24.43	10.09	5.13
8	47.00	8.00	30.00	10.00	5.00	L + CT	—	—	—	—	—
9	46.00	10.00	29.00	10.00	5.00	L + CT	—	—	—	—	—
10	47.00	11.00	27.00	10.00	5.00	L + CT	—	—	—	—	—
11	39.00	10.00	36.00	10.00	5.00	L + CT	—	—	—	—	—
12	35.00	10.50	39.50	10.00	5.00	L + CT	—	—	—	—	—
13	35.50	21.50	28.00	10.00	5.00	L	35.65	21.85	27.35	10.12	5.03
14	38.25	20.59	26.16	10.00	5.00	L	38.11	20.78	25.95	10.07	5.09
15	38.25	19.83	26.92	10.00	5.00	L	38.02	20.13	26.88	9.95	5.02
16	42.50	18.70	23.80	10.00	5.00	L	42.59	19.09	23.33	10.02	4.97
17	41.00	18.50	25.50	10.00	5.00	L	41.22	18.76	24.85	10.11	5.06
18	45.00	15.60	24.40	10.00	5.00	L	44.77	16.06	23.99	10.10	5.08

\*liquid, \*\*perovskite.



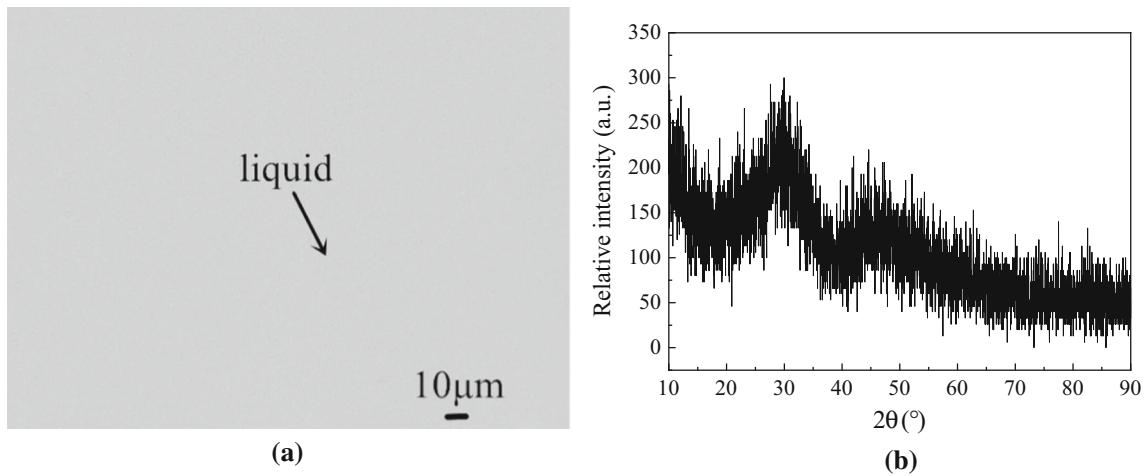


Fig. 2—An example result indicating the only existence of liquid at 1773 K in the liquid phase region (example sample: 41 wt pct  $\text{TiO}_2$ -25.5 wt pct  $\text{CaO}$ -18.5 wt pct  $\text{SiO}_2$ -10 wt pct  $\text{Al}_2\text{O}_3$ -5 wt pct  $\text{MgO}$ ), (a) SEM-BSE micrograph, (b) XRD pattern.

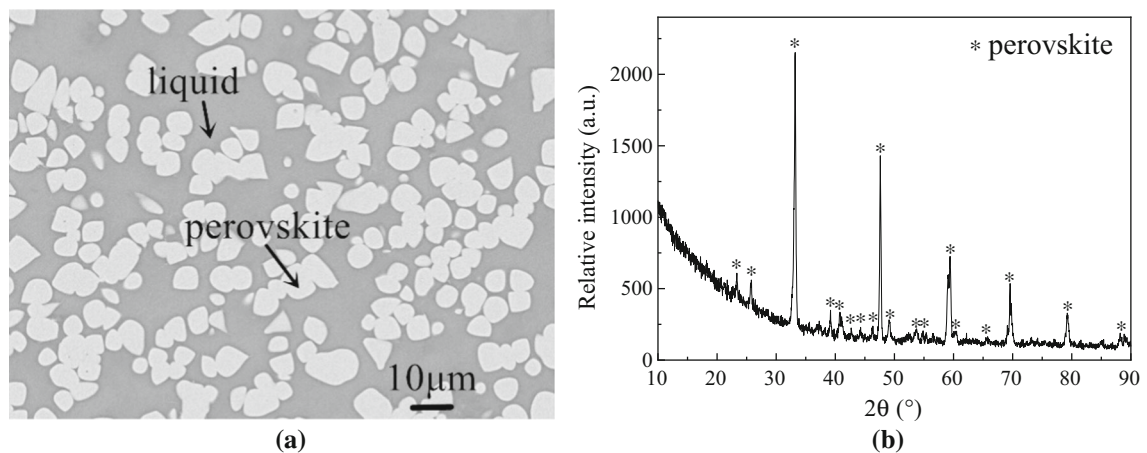


Fig. 3—An example result indicating the liquid-perovskite coexistence equilibrium at 1773 K in the primary phase region of perovskite (example sample: 46 wt pct  $\text{TiO}_2$ -29 wt pct  $\text{CaO}$ -10 wt pct  $\text{SiO}_2$ -10 wt pct  $\text{Al}_2\text{O}_3$ -5 wt pct  $\text{MgO}$ ), (a) SEM-BSE micrograph, (b) XRD pattern.

large amount of perovskite leads to the content of  $\text{Al}_2\text{O}_3$  and  $\text{MgO}$  in glass phase dramatically deviating from 10 and 5 pct respectively, so it is meaningless to be subjected to the EPMA analysis for these samples. Actually, samples Nos. 8 to 12 are mainly used to identify the phase boundary among primary phase region of perovskite and other liquid–solid co-existing regions. The compositions of the quenched glass phase obtained by EPMA in Table I are calculation values as the average of 6 different analysis points (within 0.8  $\delta$  uncertainty) in each sample.

In fact, to determine the liquid line in the primary phase region of perovskite accurately, in the preparation of samples, an experimental point was firstly selected near the 1773 K isotherm in the phase diagram of  $\text{TiO}_2$ - $\text{CaO}$ - $\text{SiO}_2$ -10 wt pct  $\text{Al}_2\text{O}_3$  system reported in our another work.<sup>[29]</sup> And then 5 wt pct  $\text{MgO}$  was added with corresponding composition adjustments of  $\text{TiO}_2$ ,  $\text{CaO}$ , and  $\text{SiO}_2$ . By this method, the liquidus temperature of the prepared sample would be close to 1773 K more likely. Based on the phase equilibrium

result of this first selected experimental point, another experimental point closer to liquid line can be selected to make sure that trace amount of perovskite can be detected and minor  $\text{MgO}$  and  $\text{Al}_2\text{O}_3$  content deviations from 5 and 10 wt pct.

To sum up, according to the results in Table I, the primary phase region of perovskite can be determined in  $\text{TiO}_2$ -rich part of the  $\text{TiO}_2$ - $\text{CaO}$ - $\text{SiO}_2$ -10 wt pct  $\text{Al}_2\text{O}_3$ -5 wt pct  $\text{MgO}$  system at 1773 K.

#### D. Primary Phase Region of Anosovite

Table II shows the compositions of the experimental samples, the glass phase composition obtained by EPMA in each quenched sample, and the phases found in the primary phase region of anosovite at 1773 K. A total of 22 samples were studied in the present phase region, containing 6 liquid samples and 16 liquid-anosovite co-existing samples. Similarly to the primary phase region of perovskite, an example (sample: 60 wt pct  $\text{TiO}_2$ -15.2 wt pct  $\text{CaO}$ -9.8 wt pct  $\text{SiO}_2$ -10 wt pct

**Table II. Compositions of the Experimental Samples and the Glass Phase in Some Quenched Samples in the Primary Phase Region of Anosovite**

Nos.	Composition of the Experimental Sample (Weight Percent)					Phases Present	Glass Phase Composition Obtained by EPMA in Each Quenched Sample (Weight Percent)				
	TiO <sub>2</sub>	SiO <sub>2</sub>	CaO	Al <sub>2</sub> O <sub>3</sub>	MgO		TiO <sub>2</sub>	SiO <sub>2</sub>	CaO	Al <sub>2</sub> O <sub>3</sub>	MgO
19	46.50	17.00	21.50	10.00	5.00	L + A*	45.14	17.23	22.41	10.14	5.08
20	44.20	21.00	19.80	10.00	5.00	L + A	42.50	21.97	20.53	10.07	4.93
21	42.00	24.50	18.50	10.00	5.00	L + A	40.52	25.46	19.05	10.01	4.96
22	40.00	28.50	16.50	10.00	5.00	L + A	38.24	29.29	16.96	10.42	5.09
23	37.60	32.00	15.40	10.00	5.00	L + A	37.12	32.13	15.73	9.96	5.06
24	37.00	35.00	13.00	10.00	5.00	L + A	35.70	35.76	13.35	10.09	5.10
25	36.00	37.70	11.30	10.00	5.00	L + A	34.96	38.69	11.37	9.97	5.01
26	47.30	15.00	22.70	10.00	5.00	L + A	46.29	15.20	23.22	10.22	5.08
27	50.00	15.00	20.00	10.00	5.00	L + A	—	—	—	—	—
28	60.00	9.80	15.20	10.00	5.00	L + A	—	—	—	—	—
29	65.00	7.50	12.50	10.00	5.00	L + A	—	—	—	—	—
30	68.00	7.00	10.00	10.00	5.00	L + A	—	—	—	—	—
31	65.00	10.00	10.00	10.00	5.00	L + A	—	—	—	—	—
32	77.00	5.00	3.00	10.00	5.00	L + A	—	—	—	—	—
33	55.00	28.00	2.00	10.00	5.00	L + A	—	—	—	—	—
34	45.00	40.00	0.00	10.00	5.00	L + A	—	—	—	—	—
35	45.50	17.00	22.50	10.00	5.00	L	45.11	17.30	22.21	10.27	5.11
36	40.50	25.00	19.50	10.00	5.00	L	40.35	25.34	19.16	9.99	5.16
37	38.50	28.50	18.00	10.00	5.00	L	38.66	28.87	17.41	10.10	4.96
38	36.80	32.00	16.20	10.00	5.00	L	36.57	32.45	15.63	10.32	5.03
39	35.00	35.00	15.00	10.00	5.00	L	35.09	35.33	14.42	10.06	5.10
40	34.20	39.00	11.80	10.00	5.00	L	34.04	39.46	11.68	9.93	4.89

\*anosovite.

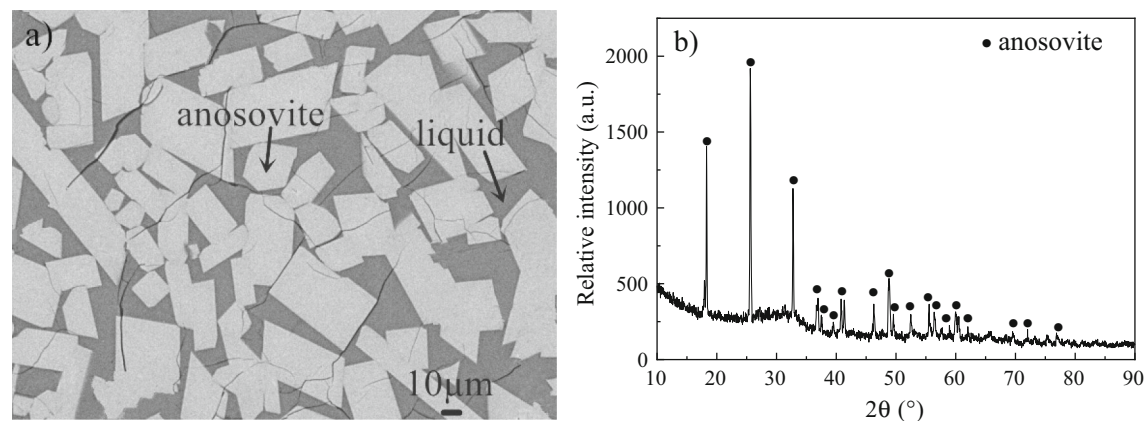


Fig. 4—An example result indicating the liquid-anosovite coexistence equilibrium at 1773 K in the primary phase region of anosovite (example sample: 60 wt pct TiO<sub>2</sub>-15.2 wt pct CaO-9.8 wt pct SiO<sub>2</sub>-10 wt pct Al<sub>2</sub>O<sub>3</sub>-5 wt pct MgO), (a) SEM-BSE micrograph, (b) XRD pattern.

Al<sub>2</sub>O<sub>3</sub>-5 wt pct MgO) of the SEM-BSE micrograph and the XRD pattern for liquid-anosovite coexistence equilibrium at 1773 K is presented in Figure 4. In Figure 4, the light grey phase is identified as anosovite based on a combination analysis of the SEM-EDS and the XRD results, and the dark grey phase is designated as the quenched glass phase. The SEM-EDS result for the light grey phase in Figure 4 is presented in Table III to show the exact composition of anosovite phase. It can be seen that the content of Ti is high, which is favorable to increase the TiO<sub>2</sub> level of the final product by selective separation of anosovite. Combined with the valence

**Table III. The Exact Composition of Anosovite Phase (Weight Percent)**

O	Ti	Mg	Al
40.06	49.35	6.99	3.59

state of titanium element, it can be known that there are three endmembers (MgTi<sub>2</sub>O<sub>5</sub>, Al<sub>2</sub>TiO<sub>5</sub>, and Ti<sub>3</sub>O<sub>5</sub>) in anosovite solid solution.

Similar to the primary phase region of perovskite, the liquid composition for each liquid-anosovite co-existing sample can be determined to identify the corresponding liquid points in the isotherm. As previously explained, in Table II, only the liquid–solid co-existing samples (Nos. 19 to 26) with trace amount of anosovite are subjected to the quantitative analysis of the quenched glass phase by EPMA to obtain the corresponding liquid points in the isotherm in this phase region. And samples Nos. 27 to 34 are mainly used to identify the phase boundary among primary phase region of anosovite and other liquid–solid co-existing regions. To sum up, according to the results in Table II, the primary phase region of anosovite can be determined in TiO<sub>2</sub>-rich part of the TiO<sub>2</sub>-CaO-SiO<sub>2</sub>-10 wt pct Al<sub>2</sub>O<sub>3</sub>-5 wt pct MgO system at 1773 K.

### E. Other Multi-phase Regions

Three multi-phase regions were also found in this system, the phase region of liquid-anosovite-perovskite, the phase region of liquid-anosovite-perovskite-spinel, and the phase region of liquid-perovskite-spinel. Table IV shows the compositions of the experimental samples and the phases found in these multi-phase regions. Examples of the SEM-BSE micrographs and

the XRD patterns for liquid-anosovite-perovskite coexistence equilibrium (sample: 48 wt pct TiO<sub>2</sub>-27.5 wt pct CaO-9.5 wt pct SiO<sub>2</sub>-10 wt pct Al<sub>2</sub>O<sub>3</sub>-5 wt pct MgO), liquid-anosovite-perovskite-spinel coexistence equilibrium (sample: 55 wt pct TiO<sub>2</sub>-27.5 wt pct CaO-2.5 wt pct SiO<sub>2</sub>-10 wt pct Al<sub>2</sub>O<sub>3</sub>-5 wt pct MgO), and liquid-perovskite-spinel coexistence equilibrium (sample: 49.5 wt pct TiO<sub>2</sub>-31.5 wt pct CaO-4 wt pct SiO<sub>2</sub>-10 wt pct Al<sub>2</sub>O<sub>3</sub>-5 wt pct MgO) at 1773 K are presented, respectively, in Figures 5, 6, and 7. Based on a combination analysis of the SEM-EDS and the XRD results in these figures, the light grey phase with a rod shape is identified as anosovite, the light grey phase with a cube-like shape is identified as perovskite, the black phase is identified as spinel, and the dark grey phase is designated as the quenched glass phase. The exact composition of anosovite phase in these regions is similar to that in Figure 4, so is not shown here.

Combined with some of the results in Tables I and IV, the phase boundary between primary phase region of perovskite and liquid-anosovite-perovskite co-existing region can be obtained by distinguishing the different crystal phases between two neighboring samples. Similarly, the phase boundary between primary phase region of anosovite and liquid-anosovite-perovskite co-existing region can also be obtained by comparing

**Table IV. Compositions of the Experimental Sample and the Phases Found in Different Phase Regions**

Nos.	Composition of the Experimental Sample (Weight Percent)					Phases Present
	TiO <sub>2</sub>	SiO <sub>2</sub>	CaO	Al <sub>2</sub> O <sub>3</sub>	MgO	
41	49.30	11.62	24.08	10.00	5.00	liquid + anosovite + perovskite
42	48.50	13.50	23.00	10.00	5.00	liquid + anosovite + perovskite
43	53.55	8.97	22.48	10.00	5.00	liquid + anosovite + perovskite
44	59.00	7.00	19.00	10.00	5.00	liquid + anosovite + perovskite
45	72.00	3.00	10.00	10.00	5.00	liquid + anosovite + perovskite
46	55.00	10.50	19.50	10.00	5.00	liquid + anosovite + perovskite
47	80.80	0.00	4.20	10.00	5.00	liquid + anosovite + perovskite
48	82.30	0.00	2.70	10.00	5.00	liquid + anosovite + perovskite
49	70.00	0.00	15.00	10.00	5.00	liquid + anosovite + perovskite
50	53.00	7.00	25.00	10.00	5.00	liquid + anosovite + perovskite
51	50.00	8.00	27.00	10.00	5.00	liquid + anosovite + perovskite
52	48.50	7.50	29.00	10.00	5.00	liquid + anosovite + perovskite
53	55.00	4.00	26.00	10.00	5.00	liquid + anosovite + perovskite
54	64.20	0.00	20.80	10.00	5.00	liquid + anosovite + perovskite
55	48.00	9.50	27.50	10.00	5.00	liquid + anosovite + perovskite
56	49.00	6.00	30.00	10.00	5.00	liquid + anosovite + perovskite + spinel
57	50.00	5.00	30.00	10.00	5.00	liquid + anosovite + perovskite + spinel
58	55.00	2.50	27.50	10.00	5.00	liquid + anosovite + perovskite + spinel
59	62.50	0.00	22.50	10.00	5.00	liquid + anosovite + perovskite + spinel
60	55.00	0.00	30.00	10.00	5.00	liquid + anosovite + perovskite + spinel
61	48.00	4.00	33.00	10.00	5.00	liquid + perovskite + spinel
62	49.50	4.00	31.50	10.00	5.00	liquid + perovskite + spinel
63	47.00	6.50	31.50	10.00	5.00	liquid + perovskite + spinel
64	45.00	5.00	35.00	10.00	5.00	liquid + perovskite + spinel
65	44.00	7.20	33.80	10.00	5.00	liquid + perovskite + spinel
66	40.00	8.00	37.00	10.00	5.00	liquid + perovskite + spinel
67	52.50	0.00	32.50	10.00	5.00	liquid + perovskite + spinel
68	53.70	0.00	31.30	10.00	5.00	liquid + perovskite + spinel
69	48.50	0.00	36.50	10.00	5.00	liquid + perovskite + spinel



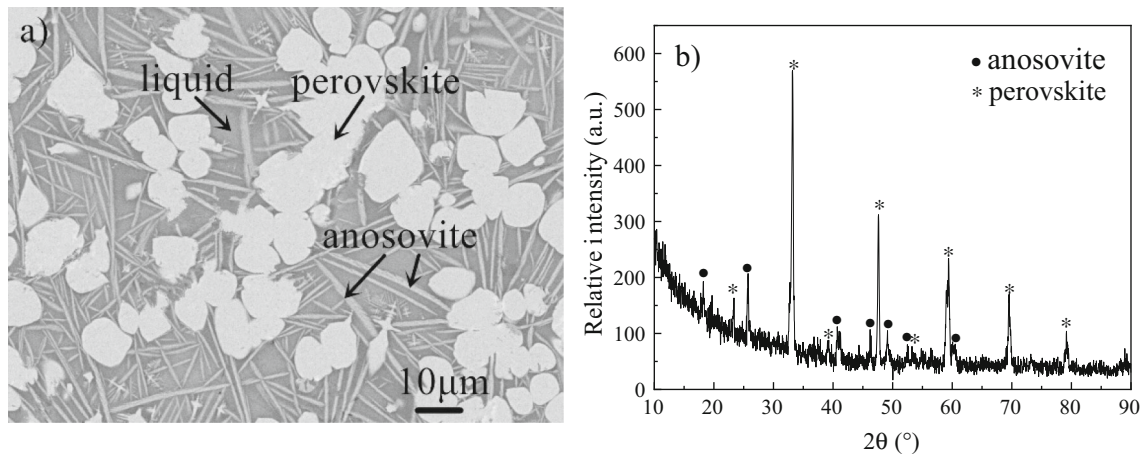


Fig. 5—An example result indicating the liquid-anosovite-perovskite coexistence equilibrium at 1773 K in the phase region of liquid-anosovite-perovskite (example sample: 48 wt pct  $\text{TiO}_2$ -27.5 wt pct  $\text{CaO}$ -9.5 wt pct  $\text{SiO}_2$ -10 wt pct  $\text{Al}_2\text{O}_3$ -5 wt pct  $\text{MgO}$ ), (a) SEM-BSE micrograph, (b) XRD pattern.

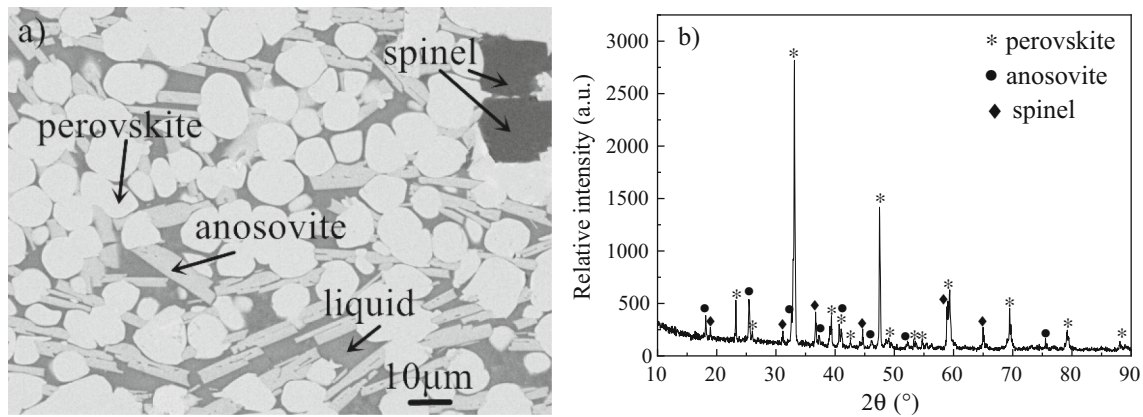


Fig. 6—An example result indicating the liquid-anosovite-perovskite-spinel coexistence equilibrium at 1773 K in the phase region of liquid-anosovite-perovskite-spinel (example sample: 55 wt pct  $\text{TiO}_2$ -27.5 wt pct  $\text{CaO}$ -2.5 wt pct  $\text{SiO}_2$ -10 wt pct  $\text{Al}_2\text{O}_3$ -5 wt pct  $\text{MgO}$ ), (a) SEM-BSE micrograph, (b) XRD pattern.

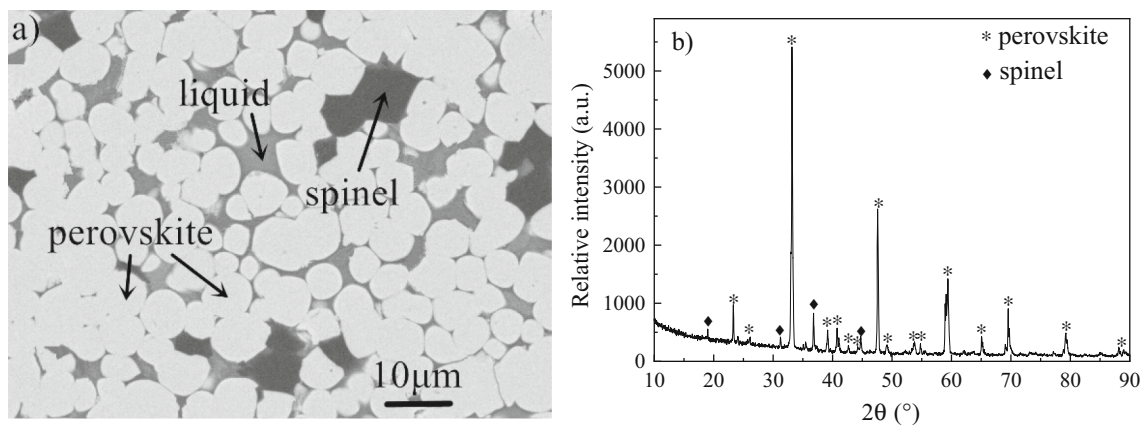


Fig. 7—An example result indicating the liquid-perovskite-spinel coexistence equilibrium at 1773 K in the phase region of liquid-perovskite-spinel (example sample: 49.5 wt pct  $\text{TiO}_2$ -31.5 wt pct  $\text{CaO}$ -4 wt pct  $\text{SiO}_2$ -10 wt pct  $\text{Al}_2\text{O}_3$ -5 wt pct  $\text{MgO}$ ), (a) SEM-BSE micrograph, (b) XRD pattern.



some of the results in Tables II and IV. And other phase boundaries can also be obtained respectively by comparing some of the results for different neighboring phase regions in Table IV.

From the above, the distribution of phase regions in the investigated system is clear. So, the phase diagram of the current system at 1773 K has been constructed according to the normalized data calculating from EPMA quantitative measurement of the glass phase and the different equilibrium state between two neighboring samples in Tables I, II, IV. The phase diagram of the  $\text{TiO}_2\text{-CaO-SiO}_2\text{-10 wt pct Al}_2\text{O}_3\text{-5 wt pct MgO}$  system in the  $\text{TiO}_2$ -rich corner at 1773 K is shown in Figure 8. From Figure 8, it can be seen that there exists a large primary phase region of anosovite. In Zhao's results, the primary phase field of anosovite is also found at high " $\text{TiO}_2$ " concentration with fixed  $\text{Al}_2\text{O}_3/\text{SiO}_2$  ratio and  $\text{MgO}/\text{CaO}$  ratio.<sup>[21]</sup> The composition range for the primary phase region of anosovite in our work is consistent with Zhao's study. And the experimental conditions of our and Zhao's work are similar (Ar + Mo crucible + carbon crucible). It is proved that the results in the current study are reliable.

Compared with the phase equilibria data in  $\text{TiO}_2\text{-CaO-SiO}_2\text{-10 wt pct Al}_2\text{O}_3$  system,<sup>[29]</sup> the results in this work reinforce suggestions that MgO is a critical component to stabilize the anosovite phase. According to Wen's study, this may be because that the ionic radius of Mg is similar to that of Ti, and Mg is easy to enter the anosovite crystal to help the  $[\text{TiO}_6]$  octahedrons link with each other by sharing a corner so as to enhance the stability of the crystal structure.<sup>[15]</sup> This study

completely reveals the significance of MgO addition during the slag adjusting process, so as to realize the selective crystallization of anosovite.

This work aims to find out the optimal composition region for anosovite selective crystallization and separation. In Figure 8, it can be seen that there are totally three phase regions containing anosovite, liquid-anosovite-perovskite-spinel phase region, liquid-anosovite-perovskite phase region, and primary phase region of anosovite. However, based on the series of requirements for anosovite in crystal shape, particle size, grain boundary, and so on when using the selective crystallization and phase separation method,<sup>[13]</sup> only the primary phase region of anosovite is the optimal region. From Figures 4, 5, and 6, it can be seen that anosovite precipitated in the primary phase region of anosovite shows relatively large size and simple grain boundaries which is beneficial to the application of the selective crystallization and phase separation method. While in the liquid-anosovite-perovskite-spinel phase region and liquid-anosovite-perovskite phase region, on one hand, anosovite is not the dominant crystal phase and a large amount of Ti component is wastefully concentrated in perovskite which is not the suitable phase for the selective crystallization and phase separation method. On the other hand, in this two phase regions, it can be seen from Figures 5 and 6 that anosovite particle is in small size which is unfavorable to the selective crystallization and phase separation method. So, it is advisable to take the primary phase region of anosovite as the optimal composition region to guide the slag composition adjustment during the smelting process of vanadium-titanium magnetites.

The present study greatly enriches the phase equilibria data of the Ti-bearing slag system with high  $\text{TiO}_2$  content. The obtained phase diagram can serve as the guideline for the slag composition optimization during the smelting process of vanadium-titanium magnetites.

#### IV. CONCLUSIONS

The phase equilibria in the  $\text{TiO}_2$ -rich part of the  $\text{TiO}_2\text{-CaO-SiO}_2\text{-10 wt pct Al}_2\text{O}_3\text{-5 wt pct MgO}$  system at 1773 K were experimentally investigated by the quenching method and EPMA analysis. One liquidus region, five solid-liquid coexistence regions (liquid-perovskite, liquid-anosovite, liquid-anosovite-perovskite, liquid-anosovite-perovskite-spinel and liquid-perovskite-spinel) were obtained. As expected, the primary phase region of anosovite was found and the optimal composition region for anosovite selective crystallization and separation was identified. The phase diagram was constructed in the  $\text{TiO}_2$ -rich corner of the  $\text{TiO}_2\text{-CaO-SiO}_2\text{-10 wt pct Al}_2\text{O}_3\text{-5 wt pct MgO}$  system at 1773 K. The phase diagram clearly presents the optimal composition region as the guideline for adjusting the composition of the Ti-bearing slag during the smelting process to ensure the crystallization of the anosovite.

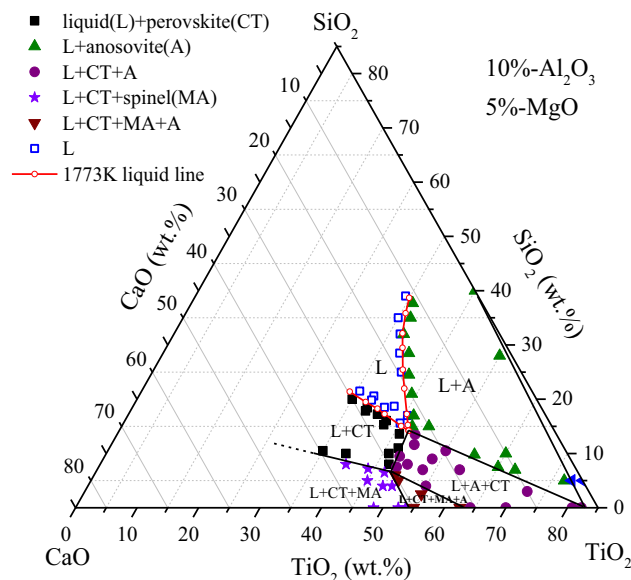


Fig. 8—Phase diagram of the  $\text{TiO}_2\text{-CaO-SiO}_2\text{-10 wt pct Al}_2\text{O}_3\text{-5 wt pct MgO}$  system in the  $\text{TiO}_2$ -rich corner at 1773 K.

## ACKNOWLEDGMENTS

The authors are grateful to financial support from the National Natural Science Foundation of China (Nos. 51404226 and 21736010).

## REFERENCES

1. J. Li, Z.T. Zhang, and X.D. Wang: *Ironmak. Steelmak.*, 2012, vol. 6, pp. 414–18.
2. J. Li, Z.T. Zhang, M. Zhang, M. Guo, and X.D. Wang: *Steel Res. Int.*, 2011, vol. 82, pp. 607–14.
3. M.Y. Wang, L. Zhang, Z.T. Sui, X.W. Wang, and Y.H. He: *Ironmak. Steelmak.*, 2009, vol. 36, pp. 388–92.
4. L. Zhang, L.N. Zhang, M.Y. Wang, T.P. Lou, Z.T. Sui, and J.S. Jang: *J. Non-Cryst. Solids*, 2006, vol. 352, pp. 123–29.
5. A. Ohno and H.U. Ross: *Can. Metall. Q.*, 1963, vol. 3, pp. 259–79.
6. M.T. Gueguin: Chlorine, hydrochloric acid, *US Patent 5063032*, 1991.
7. J.P. Van Dyk and P.C. Pistorius: *Metall. Mater. Trans. B*, 1999, vol. 30B, pp. 823–26.
8. K.S. Kamala, C.A. Thomas, M. Devabrata, and A. Archana: *Waste Manage. Res.*, 2006, vol. 24, pp. 74–79.
9. X.D. Wang, Y.W. Mao, X.Y. Liu, and Y.K. Zhu: *J. Iron Steel Res.*, 1990, vol. 3, pp. 1–6.
10. P.X. Zhang, Z.T. Sui, D.M. Luo, and J.R. Ma: *Chin. J. Mater. Res.*, 1995, vol. 1, pp. 66–70.
11. X.R. Wu, L.S. Li, and Y.C. Dong: *ISIJ Int.*, 2007, vol. 3, pp. 402–07.
12. Y.H. Li, T.P. Lou, and Z.T. Sui: *Chin. J. Nonferrous Met.*, 2000, vol. 5, pp. 719–22.
13. Z. Wang, X.W. Liu, L. Zhang, and Q.S. Zhu: *Trans. Indian Inst. Met.*, 2016, vol. 69, pp. 97–105.
14. H.H. William and M.I. Douglas: Production of anosovite from titaniferous minerals, *U.S. Patent 3502460*, 1970.
15. Y.J. Wang, S.M. Wen, Q.C. Feng, J. Liu, and W.C. Ren: *Trans. Nonferrous Met. Soc. China*, 2016, vol. 26, pp. 2518–22.
16. Y.J. Wang, Y.J. Xian, S.M. Wen, J.S. Deng, and D.D. Wu: *J. Alloys Comp.*, 2017, vol. 708, pp. 982–88.
17. D. Xirouchakis, A. Smirnov, K. Woody, D.H. Lindsley, and D.J. Andersen: *Am. Mineral.*, 2002, vol. 87, pp. 658–67.
18. S. Seim and L. Kolbeinsen: *Heavy Minerals Conf.*, 2009, pp. 57–62.
19. B.J. Yan, X. Wang, and Z.B. Yang: *J. Alloys Comp.*, 2017, vol. 695, pp. 3476–83.
20. X. Goso, J. Nell and J. Petersen: *Advances in Molten Slags, Fluxes, and Salts: 10th Int. Conf. Molten Slags, Fluxes and Salts*, 2016, pp. 105–14.
21. B.J. Zhao, E. Jak, and P.C. Hayes: *J. Iron Steel Res.*, 2009, vol. 16, pp. 1172–78.
22. E.F. Osborn and K.H. Gee: *Bull. Earth Miner. Sci. Exp. Stn.*, 1969, vol. 85, pp. 57–80.
23. J.J. Shi, L.F. Sun, B. Zhang, X.Q. Liu, J.Y. Qiu, Z.Y. Wang, and M.F. Jiang: *Metal. Mater. Trans. B*, 2016, vol. 47, pp. 425–33.
24. J.J. Shi, L.F. Sun, J.Y. Qiu, and M.F. Jiang: *ISIJ Int.*, 2018, vol. 58, pp. 431–38.
25. J.J. Shi, L.F. Sun, J.Y. Qiu, and M.F. Jiang: *J. Alloys Comp.*, 2017, vol. 722, pp. 25–32.
26. I.P. Ratchev and G.R. Belton: *5th Int. Conf. Molten Slags, Fluxes and Salts*, 1997, pp. 387–93.
27. W.T. Holmes, L.H. Banning and L.L. Brown: *US Dept. of the Inter. Bur. Mines*, 1968, vol. 1, pp. 1–21.
28. E. Jak, P.C. Hayes, and H.G. Lee: *Met. Mater.*, 1995, vol. 1, pp. 1–8.
29. Z. Wang, H.Y. Sun, L. Zhang, and Q.S. Zhu: *J. Alloys Comp.*, 2016, vol. 671, pp. 137–43.